Volume 21
Number 48
28 December 2025
Pages 9175–9414

Soft Matter

rsc.li/soft-matter-journal

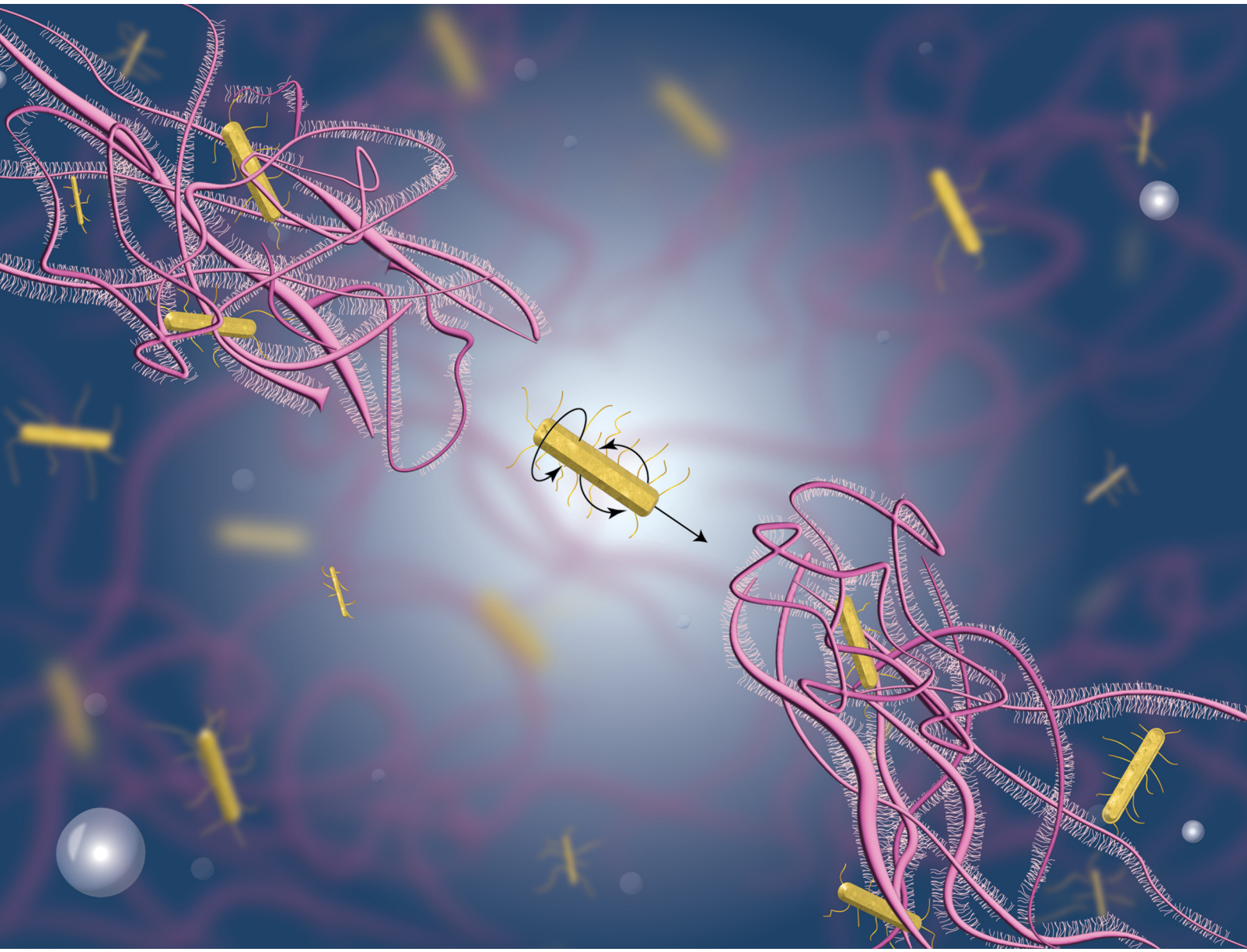

ISSN 1744-6848

ROYAL SOCIETY OF CHEMISTRY

PAPER
Mary Mel Balacuit Baynosa and Ashis Mukhopadhyay
Transient interactions and local heterogeneity drive rotational–translational decoupling of nanorods in semidilute mucin solutions

20 YEARS ANNIVERSARY

Soft Matter

PAPER

View Article Online
View Journal | View Issue

Check for updates

Cite this: *Soft Matter*, 2025, **21**, 9203

Transient interactions and local heterogeneity drive rotational–translational decoupling of nanorods in semidilute mucin solutions

Mary Mel Balacuit Baynosa and Ashis Mukhopadhyay *

Received 21st July 2025,
Accepted 17th September 2025

DOI: 10.1039/d5sm00742a

rsc.li/soft-matter-journal

We investigated the rotational and translational dynamics of gold nanorods in semidilute solutions of bovine submaxillary mucin (BSM), a biologically relevant bottlebrush polymer rich in MUC5B. Using fluctuation correlation spectroscopy (FCS), we observe that both translational and rotational motions exhibit anomalous subdiffusion, with the corresponding exponents decreasing systematically with mucin concentration. Mean-square displacement (MSD) analysis reveals a clear crossover from short-time subdiffusion to long-time normal diffusion at low mucin levels, while persistent subdiffusion dominates at higher concentrations. Translational diffusion coefficients show only weak dependence on polymer volume fraction, whereas rotational mobility is markedly constrained, particularly at elevated mucin volume fractions. These results cannot be fully explained by conventional hydrodynamic or obstruction-based theories. Instead, we attribute the observed decoupling between translation and rotation to transient interactions between nanorods and mucin chains, combined with spatial heterogeneity in local polymer density and segmental dynamics. Our findings demonstrate how anisotropic probes can sensitively capture multiscale viscoelastic and structural features of complex biological polymer solutions.

Open Access Article. Published on 18 September 2025. Downloaded on 2/18/2026 8:59:30 PM.
This article is licensed under a Creative Commons Attribution-NonCommercial 3.0 Unported Licence.

1. Introduction

Understanding nanoparticle transport in complex biological environments is essential for the rational design of targeted drug delivery systems, high-sensitivity diagnostics, and effective therapeutics.[1–6] These applications rely on the ability of nanoscale entities—ranging from proteins to synthetic particles—to traverse extracellular barriers such as mucus, which presents unique physical and biochemical challenges.[7–11] Mucus is a viscoelastic, entangled hydrogel that lines the respiratory, gastrointestinal, and reproductive tracts.[12] It serves multiple physiological functions, including hydration, lubrication, nutrient exchange, and immune defense.[8–10,13] In the respiratory system, mucus captures pathogens and environmental particulates, preventing their access to epithelial surfaces.[10,13]

Structurally, mucus is composed of ~95 wt% water and ~5 wt% solids, including mucins, salts, proteins, and lipids.[14] Despite their low mass fraction, mucins—large, heavily glycosylated proteins—are the primary determinants of mucus viscoelasticity.[14] These proteins form bottlebrush-like architectures with dense sugar side chains and terminal domains capable of forming disulfide crosslinks.[14,15] Together with noncovalent interactions, these structural features promote the formation of a heterogeneous and dynamic polymer mesh that underlies the barrier properties of mucus.[14]

In humans, mucus is part of the airway surface liquid (ASL), which consists of a high-viscosity mucus gel layer overlaying a low-viscosity periciliary layer (PCL).[13] While prior work has focused on bulk rheological characterization of mucus and its barrier property at the microscale,[7,10,11] its nanoscale barrier properties—especially in relation to mucin concentration, microstructure, and particle geometry—remain incompletely understood. Our previous study using reconstituted mucin gels demonstrated that nanoscale diffusion is strongly influenced by transient mesh fluctuations, heterogeneities in the polymer network, and interstitial fluid properties.[16] These systems primarily model the mucus gel layer. In contrast, the PCL has lower mucin content and a viscosity closer to that of water. Since nanoparticles may encounter both environments *in vivo*, characterizing their transport behavior across a range of mucin concentrations is critical for understanding and overcoming mucus-mediated barriers.

Another motivation for this study is that many naturally occurring and synthetic nanoparticles are not spherical but instead exhibit irregular or anisotropic shapes. Unlike spheres, rods undergo anisotropic diffusion due to their geometry and associated rotational degrees of freedom. The theoretical

Department of Physics, Wayne State University, Detroit, MI 48201, USA.
E-mail: ashis@wayne.edu

Open Access Article. Published on 18 September 2025. Downloaded on 2/18/2026 8:59:30 PM. This article is licensed under a Creative Commons Attribution-NonCommercial 3.0 Unported Licence.

studies have established the importance of aspect ratio, entanglement, and network interactions in governing transport and behavior.[17,18] Previous experimental research using depolarized dynamic light scattering (DDLS) of rodlike biomacromolecules, such as Tobacco mosaic virus (TMV) in concentrated dextran solutions revealed simultaneous slowing of translational and rotational diffusion, along with deviations from Stokes–Einstein scaling at high concentrations.[19] More recently, investigations of rodlike nanoparticles in polymeric and biological networks have highlighted anomalous transport and the role of coupled rotational–translational dynamics.[11,20–22] Both simulations and experiments have further shown that rods can experience enhanced translational mobility in confined polymer networks through rotation-facilitated dynamics.[1,23–25] For example, Xue *et al.* demonstrated that rodlike nanoparticles display anomalously rapid transport in polymer gels, with a stretch exponent of 0.25 serving as a fingerprint of coupled dynamics.[26] Similarly, another study showed that cylindrical nanoparticles, such as mesoporous silica and calcium phosphate nanorods, diffuse more efficiently in mucus than spheres of the same chemistry, enabling deeper penetration and longer GI tract retention. This behavior was attributed to rotation-facilitated dynamics as verified by molecular dynamics simulation.[25] We note, however, that these two prior studies were conducted in gels with permanent mesh-like structures, whereas in our system any network formation is transient in nature, leading to qualitatively different dynamical constraints. Taken together, all these studies emphasize that rodlike geometries, which are common in biological systems, differ fundamentally from spheres, exhibiting anisotropic diffusion due to their shape and associated rotational degrees of freedom.

Here, we investigated the diffusion of gold nanorods in mucin solutions spanning physiologically relevant concentrations that model the periciliary layer. By using fluctuation correlation spectroscopy (FCS) with polarized light, we simultaneously track translational and rotational diffusion of nanorods over several orders of magnitude in timescale.[20] Our findings revealed that the conventional wisdom regarding the effect of crowding—based on studies using model polymers such as dextran[27]—breaks down in complex biological media.

2. Materials and methods

Bovine submaxillary mucin (BSM), rich in MUC5B, was purchased from Sigma-Aldrich. Mucin solutions were prepared in a buffer containing 154 mM NaCl, 3 mM $CaCl_2$, and 15 mM NaH_2PO_4 (pH ~7.4), and stirred at room temperature for 2 hours.[28] Five concentrations of mucin (w/v%) were used: 1%, 1.5%, 2%, 3%, and 4%. The corresponding volume fractions (ϕ) were 0.007, 0.011, 0.015, 0.022, and 0.03. Gold nanorods (AuNRs) with core dimensions of 10 nm × 38 nm was obtained from Nanopartz, Inc. Representative TEM micrographs of the nanoparticles, as provided by the vendor, were included (Fig. S1) to illustrate particle size and morphology. All experiments were performed using samples from the same batch to ensure consistency. Their longitudinal surface plasmon resonance (LSPR) peak is centered at 780 nm. The nanorods were coated with carboxyl-terminated polyethylene glycol (PEG, M_w = 3 kDa). As the conformation of PEG was not known, we assumed that it forms random coil with a radius of gyration estimated to be[16] $R_g \approx 2$ nm. Including the PEG shell, the hydrodynamic size of the particles is 46 nm × 18 nm, having an aspect ratio of 2.6. For simplicity, we refer to the nanorods by their core dimensions throughout this article. The PEG functionalization makes the particles negatively charged due to the presence of carboxyl moieties as evidenced by the small negative Zeta potential (Fig. S2). Approximately 20 μL of AuNR stock solution (concentration ≈76 nM) was injected into ≈300 mg of mucin solution using a microsyringe (Harvard Apparatus). Samples were loaded into a cylindrical observation chamber with a borosilicate glass bottom coverslip (thickness ~0.17 mm). The chamber was cleaned with a base bath, rinsed with distilled water, and dried prior to use. After sample loading, the chamber was sealed to minimize evaporation and mounted on a mechanical stage for optical measurements.

2.1. Experimental method

FCS was employed to measure the translational and rotational diffusion of gold nanorods (AuNRs) mixed within mucin solutions. FCS measurements were carried out using a custom-built setup integrated into an inverted optical microscope (Axiovert S200TV, Carl Zeiss). Two-photon excitation was provided by a tunable Ti:sapphire femtosecond laser (Mai Tai, Spectra-Physics), operating within the 800–920 nm range, with a pulse duration of 150 fs and a repetition rate of 80 MHz. The primary advantage of two-photon excitation lies in the lower average laser power at the sample, which minimizes photothermal effects that could otherwise influence the measurements.[29] An additional benefit of near-infrared excitation is the reduction of scattering and background fluorescence from mucin molecules, thereby improving signal quality. Compared to techniques, such as dynamic light scattering or photobleaching-based methods, reliable correlation functions can be obtained even at sub-nanomolar probe concentrations, which significantly reduces perturbation of the native polymer network. The excitation beam was focused on the sample through a high numerical aperture (NA) oil-immersion objective lens (100 ×, NA = 1.25), resulting in a confined excitation volume suitable for detecting single-particle luminescence fluctuations. Luminescence emitted from the AuNRs under two-photon excitation was collected through the same objective, reflected by a dichroic mirror and filtered to reject excitation light. A dichroic mirror (Chroma, Inc.) with a cutoff at 600 nm was used to block scattered excitation light, ensuring that only photoluminescence signals were detected. The signal was then split and directed to two single-photon counting modules (Hamamatsu) arranged in a cross-correlation configuration. Photon arrival times were recorded and processed using a commercial time-correlated single-photon counting module and correlation electronics (ISS, Champaign, IL), which generated the intensity autocorrelation functions for subsequent analysis. To increase

 This journal is © The Royal Society of Chemistry 2025

Open Access Article. Published on 18 September 2025. Downloaded on 2/18/2026 8:59:30 PM. This article is licensed under a Creative Commons Attribution-NonCommercial 3.0 Unported Licence.

the lateral extent of the excitation volume (beam waist, $2\omega_0$), the laser beam underfilled the back aperture of the objective lens by removing the beam expander from the optical path.[16] The excitation volume was calibrated using a standard solution of 100 nm polystyrene nanospheres (Polysciences, Inc.). The lateral beam waist was determined by fitting the autocorrelation function originating from the Brownian motion of the tracer. At λ = 800 nm excitation wavelength, the calibrated lateral waist was found to be approximately, $2\omega_0 \approx 1.6$ μm. Each FCS experiment was conducted at ambient temperature (~24 °C) and for each condition (mucin concentration and sample type), multiple independent measurements were recorded at different spatial locations.

3. Results and discussions

FCS captures dynamic information by analyzing fluctuations in the fluorescence signal as particles diffuse into and out of a tightly focused laser volume.[16,30,31] Although the geometric anisotropy of the nanoparticles studied here is modest, their optical anisotropy is pronounced, as the transition dipole moment aligns strongly with the nanorod's major axis. The fluorescence signal thus depends not only on position but also on orientation relative to the excitation polarization. Consequently, rotational reorientation leads to additional fluorescence fluctuations, contributing an extra decay component to the autocorrelation function.[20] The fast decay component of the correlation function was assigned to rotational diffusion, as its amplitude depended strongly on the polarization state of both the excitation and detected light. This polarization sensitivity is a hallmark of rotational dynamics and distinguishes it from purely translational or other fast fluctuation processes. Similar polarization-dependent signatures have been reported previously for nanorods with comparable aspect ratios.[32] These fluctuations, as particles rotate in the tightly focused laser volume and diffuse into and out of it, are quantified using the normalized intensity autocorrelation function, $G(\tau)$ of the photon counts (F),

$$G(\tau) = \langle \delta F(t) \delta F(t+\tau) \rangle / \langle F(t) \rangle^2 \quad (1)$$

where $\delta F(t) = F(t) - \langle F(t) \rangle$ represents deviations from the mean fluorescence intensity. For normal Brownian diffusion, the autocorrelation function (ACF) has been modeled as:

$$G(\tau) = G(\tau)_t \times (1 + G_r(\tau)) \quad (2)$$

here G_t and G_r are the translational and rotational contribution to the decay of the correlation function, and given by:

$$G_t(\tau) = G(0)/[(1 + S(\tau))] \quad (3)$$

where $S(\tau) = (\tau/\tau_c)^{\alpha}$ and

$$G_r(\tau) \approx R \exp\left(-\left(\frac{\tau}{\tau_r}\right)^{\beta}\right) \quad (4)$$

The mean residence time of the particles is approximately given by $\tau_c \approx \omega_0^2/8D$, where ω_0 is the half-width of the laser focus, D is the diffusion coefficient of the particles. The anomalous exponent, α is equal to 1 for normal diffusion, but it is generally less than one in crowded, confined medium. The equation for $G_t(\tau)$ assumed that laser focus dimension is much smaller in the plane perpendicular to the beam direction compared to parallel directions so that fluctuation of the photon counts primarily originating from two-dimensional diffusion.[33] We also tested alternative fitting approaches, including a two-component model for translational diffusion that assumed one subpopulation of nanorods diffused freely while another was bound to the polymer.[31] This did not yield any improvement in the fitting.

The fitting of the rotational correlation function, G_r assumed a stretched exponential function, known as the Kohlrausch–Williams–Watts (KWW)[34] function, where τ_r is related to the rotational diffusion coefficient *via* $D_r = 1/6\tau_r$. The prefactor, R depends upon the polarization state of the excitation and emitted light as well as on the aspect ratio of the particle.[32] The stretching exponent, where $\beta < 1$ implies a broad spectrum of relaxation times with a smaller β indicating a wider spectrum. A rod-like particle has two different translational diffusion coefficients, parallel ($D_\parallel$) and perpendicular ($D_\perp$) to the long axis. But the rotation of the particles makes motion isotropic[35] at a time scale beyond $\tau > 1/2\ D_r$, which is readily satisfied for the experiments presented here. Experimentally, in this situation, the center-of-mass translational diffusion coefficient (D_t) in the laboratory frame was measured,[36] where $D_t = (D_\parallel + 2D_\perp)/3$. This averaging is correct in continuous homogeneous media but can break down in the system studied here.

Fig. S3 showed the representative autocorrelation function of nanorods diffusing in water. Here, both $\alpha, \beta \approx 1$, as expected for normal diffusion. The fitting of the ACF gives average translational diffusion coefficient, $D_t = \omega_0^2/8\tau_c \approx 16\ \mu m^2\ s^{-1}$ and the rotational diffusion coefficient, $D_r = 1/6\tau_r \approx 35\,460\ s^{-1}$. This matches very well with Tirado and Garcia de la Torre's (TT) relations of diffusion coefficient of a cylindrical shaped particle with flat ends[35] by assuming that hydrodynamic size of the particle is given by 44 nm x 16 nm, including the PEG coating.

Fig. 1 showed autocorrelation functions for five different mucin solutions. For each sample, the measurements were repeated several times for each sample and by fitting the functions, four quantities (τ_c, τ_r, α, and β) were determined. We defined a model-independent translational and rotational correlation times, which are calculated by using $\langle \tau_c \rangle = \frac{\tau_c}{\alpha} \Gamma\left(\frac{1}{\alpha}\right)$ and $\langle \tau_r \rangle = \frac{\tau_r}{\beta} \Gamma\left(\frac{1}{\beta}\right)$. Here, Γ is the Gamma function. In Fig. 2, we have shown the box-whisker plots of normalized correlation times with respect to their values in neat buffer and the associated anomalous exponents as a function of mucin volume fraction in semi-log plot. As evident from Fig. 2, all measured dynamical parameters exhibit substantial variability, even within mucin solutions at fixed concentrations. This variability may originate from intrinsic microscale heterogeneities (*e.g.*, formation of nanogel, clusters, *etc.*), fluctuations in polymer density, *etc.* Among the extracted quantities, the translational

Open Access Article. Published on 18 September 2025. Downloaded on 2/18/2026 8:59:30 PM.
This article is licensed under a Creative Commons Attribution-NonCommercial 3.0 Unported Licence.

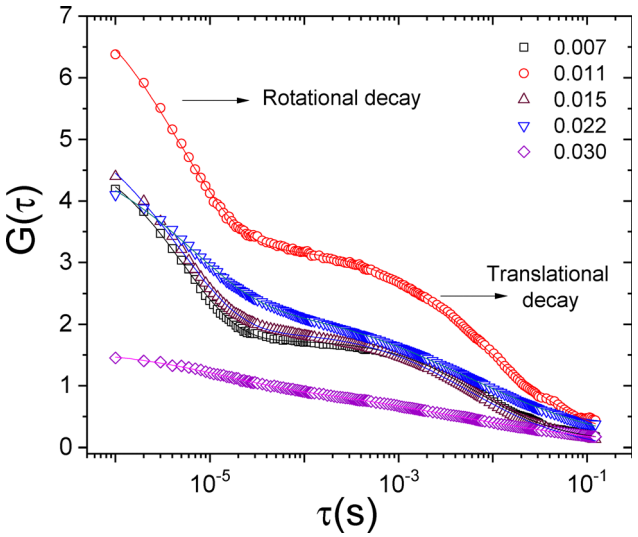

Fig. 1 Representative autocorrelation functions (ACFs) of gold nanorods with core dimensions of 10 nm × 38 nm, dispersed in bovine submaxillary mucin (BSM) solutions. (graphs are vertically shifted for clarity) The nanorods were surface-functionalized with 3 kDa PEG–carboxyl ligands. The volume fractions (ϕ) of mucin are indicated. The ACFs exhibit two-step decay: the fast decay corresponds to rotational motion, while the slower decay reflects translational diffusion. Solid lines represent fits using the model described in the main text, yielding the mean residence time within the confocal volume ($\langle\tau_c\rangle$), the rotational correlation time ($\langle\tau_r\rangle$), and the associated anomalous diffusion exponents α and β.

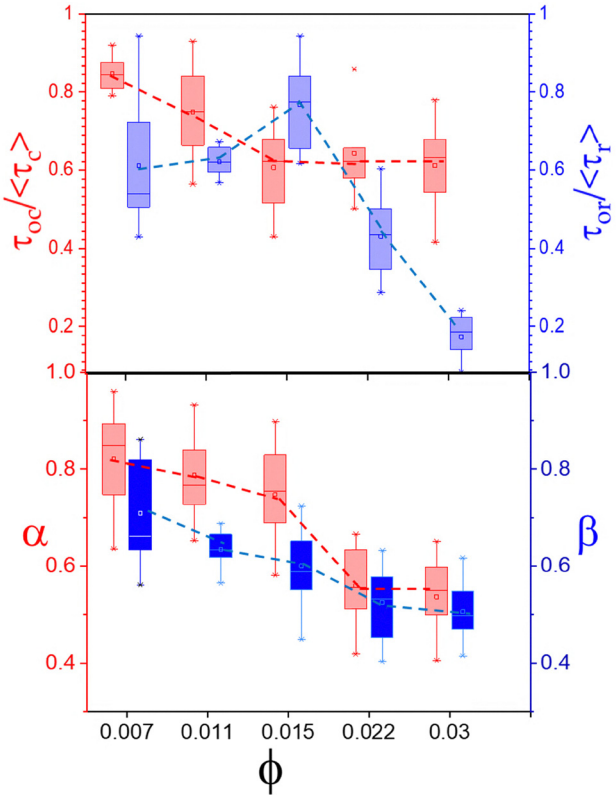

Fig. 2 (top) Box-and-whisker plots showing the mean residence times for translational diffusion (left axis) and rotational correlation times (right axis) of nanorods in BSM solutions. All values are normalized to their respective measurements in buffer ($\tau_{oc} \approx 4.9$ ms, $\tau_{or} \approx 4.7$ μs). Dashed lines are included to guide the eye. (bottom) The anomalous exponents, rather than the absolute timescales of motion, associated with translation (α, left) and rotation (β, right). A strong subdiffusive behavior emerges at higher concentrations. At the highest volume fractions, translational exponents approach $\alpha \approx 0.5$, consistent with Rouse-like dynamics.

correlation time, which is inversely related to the translational diffusion coefficient, shows only a weak and non-monotonic dependence on mucin concentration. Across the studied range of volume fractions, the reduction in translational mobility remains relatively modest, typically between 0.6 and 0.8 compared to the buffer, and does not scale strongly with mucin concentration. In contrast, rotational diffusion exhibits a sharper suppression, indicating stronger local confinement or hindrance to angular reorientation. This decoupling of translation and rotation becomes more pronounced at higher mucin concentrations and is consistent with nanorods probing more restrictive local environments rotationally than translationally. The apparent non-monotonic behavior of rotational diffusion at lower mucin concentration is intriguing and may indicate a crossover between different concentration regimes. To further examine this effect, we are conducting experiments with rods of varying aspect ratios, which are expected to provide additional insight.

Furthermore, both anomalous diffusion exponents—α for translational motion and β for rotational motion—decrease monotonically with increasing mucin content. This shift signifies stronger deviation from normal Brownian motion. Additionally, while the mean values shift, the widths of the distributions remain relatively constant, suggesting that while the average dynamics become more subdiffusive, the degree of dynamical heterogeneity does not significantly increase. At lower mucin volume fractions ($\phi < 0.011$), nanorods display only weakly anomalous behavior, with $\alpha > 0.7$, indicative of near-diffusive motion. However, as the concentration increases beyond this threshold, the motion becomes strongly subdiffusive ($\alpha < 0.6$), pointing to enhanced caging or transient binding effects in the increasingly crowded mucin environment.

We did not attempt to apply any rheological model to these data as previous studies have shown that the probe size must be several times larger than the largest structural length scale of the medium in order to couple effectively to its longest relaxation modes.[37–39] Since the tracer particles used here are much smaller, their dynamics do not directly reflect the bulk rheology. Obstruction effects and geometric constraints due to molecular crowding can cause both subdiffusion and slowdown of mobility of tracer particles.[1,40] Some experiments and simulations even suggested that the anomalous diffusion exponent serves as a sensitive indicator of crowding and heterogeneity in biological environments.[41–43] The observed trend in our experiments for α is therefore consistent with increasing microstructural constraints and crowding within the mucin network at higher concentration. Obstruction models like the Ogston theory treat polymers as static, randomly distributed obstacles reducing available volume, which can account for moderate decreases in translational diffusion but neglect dynamic polymer conformations and anisotropic

 This journal is © The Royal Society of Chemistry 2025

Open Access Article. Published on 18 September 2025. Downloaded on 2/18/2026 8:59:30 PM. This article is licensed under a Creative Commons Attribution-NonCommercial 3.0 Unported Licence.

constraints.[40,44] Hydrodynamic effects can also result in reduced mobility, from an increased friction coefficient on the particle due to no-slip boundary conditions at the large molecule surface.[3,45] In majority of models, the reduced particle mobility is given by $D/D_0 = \exp(-\kappa\phi^{\nu})$, where D_0 is the particle mobility in the neat solvent, and κ, ν are empirical fitting parameters.[40,46,47] These are inadequate as they predict that both D_t and D_r would decrease smoothly with polymer concentration. Additionally, these theories do not consider polymer semi flexibility, local crowding, and scale-dependent confinement, which can result in stretched exponential relaxation.

It is pertinent to highlight key physicochemical characteristics of mucin relevant to this study. Bovine submaxillary mucin (BSM, Type IS) obtained from Sigma-Aldrich is predominantly composed of MUC5B, a heavily glycosylated high-molecular-weight glycoprotein that constitutes the major structural and functional component of healthy respiratory mucus.[15,28,48] The hydrodynamic size distribution of mucin molecules was characterized using dynamic light scattering (DLS) in a calcium-containing buffer, revealing a monomodal distribution with hydrodynamic diameter ($2R_h$) ranging from approximately 50 to 110 nm and a modal peak centered near 80 nm (Fig. S4). Prior studies employing UV circular dichroism spectroscopy have demonstrated that MUC5B adopts a compact tertiary conformation under acidic pH and elevated Ca^{++} concentrations, whereas it assumes a more extended conformation at neutral pH.[15,48] Structurally, mucin molecules exhibit a bottlebrush architecture, wherein densely glycosylated segments have increased rigidity,[15,48] characterized by a high persistence length (compared to most synthetic polymers) on the order of 10–20 nm, while the less glycosylated segments exhibit greater flexibility with persistence lengths around 7 nm. This heterogeneous segmental flexibility profoundly influences mucin's overall conformational dynamics and interaction with tracer particles in solution.

Natural mucin extracted from bovine submaxillary glands has high molecular weight (typically >4 MDa). In contrast, reconstituted mucin from Sigma-Aldrich exhibits a lower molecular weight[48] in the range of approximately 0.8–2 MDa, with a protein backbone of $\sim$110 kDa. To estimate the overlap volume fraction for mucin, we used the standard expression for linear polymers, $\phi^* = 3M_w/(4\pi\rho N_A R_g^3)$, where ρ is the density of mucin, R_g is the radius of gyration, and N_A is the Avogadro number. Using an empirical relation for flexible-to semirigid polymer, $R_g \approx R_h/0.77$, we estimated that $2R_g \approx 104$ nm. Considering only the protein backbone molecular weight, we estimated that $\phi^* \approx 2 \times 10^{-5}$. This extremely low overlap volume fraction implies that mucin molecules begin to interpenetrate at very low concentrations, and all of our experiments were performed in the semidilute regime. However, the molecules are likely to remain unentangled. Unlike high molecular weight linear polymers, which readily form entanglements at elevated concentrations,[49] mucin's heavily glycosylated side chains increase excluded volume while simultaneously suppressing chain flexibility and interpenetration. As a result, topological entanglement between mucin molecules is unlikely, even at concentrations where linear polymers would typically exhibit entangled behavior. Therefore, while mucin chains interpenetrate and produce crowding effects characteristic of semidilute solutions, they do not form a continuous transient network.

In this semidilute-but-unentangled regime, the nanorods can still navigate through transient voids and pores created by the overlapping but loosely arranged mucin chains. This is consistent with the observed weak dependence of translational diffusion coefficients on mucin concentration. In contrast, rotation is inherently more sensitive to local microstructural constraints. The bulky glycosylated side chains of mucin increase local crowding and impose anisotropic steric barriers that disproportionately affect rotational degrees of freedom compared to translation. This manifests experimentally as a more systematic decrease in rotational diffusion coefficients with increasing polymer concentration.

In addition to extracting diffusion coefficients and anomalous exponents from the FCS measurements, the translational decay of the autocorrelation function can be inverted to yield the mean-square displacement (MSD) as a function of lag time τ by using the relation: $\langle r^2(\tau)\rangle = \frac{\omega_0^2}{2}\left(\frac{G(0)}{G_t(\tau)} - 1\right)$. As shown in Fig. 3, for the three lowest mucin concentrations, the MSD curves exhibit subdiffusive behavior at short times followed by a crossover to near-normal diffusion at longer times. This crossover behavior is not captured by the traditional fitting of the FCS curves using only two fitting parameters τ_c and α, highlighting the value of direct MSD reconstruction.[27,30,50,51] The crossover time scale, τ_x overall shifts to longer lag times with increasing mucin concentration, and for the two highest concentrations, no crossover is observed within the experimental time window—implying that τ_x exceeds the accessible dynamic range. The crossover time increases from a few milliseconds to over ten milliseconds with increasing ϕ. At short timescales, the MSD follows a power-law form $\langle r^2(\tau)\rangle \sim t^{\mu}$, with the exponent μ reflecting the degree of subdiffusion (Fig. 3, inset). For lower volume fractions (ϕ = 0.007, 0.011, and 0.015), we find $\mu \approx 0.8$ indicative of modest subdiffusive dynamics. At higher concentrations μ decreases to $\approx$0.55.

A crossover from subdiffusive to normal diffusive behavior in the MSD has been previously observed for probe particles in a variety of crowded or structurally heterogeneous media, including colloidal suspensions,[52] agarose gels,[50] and entangled actin network.[53] This behavior is often attributed to transient caging effects, where particles are locally confined within mesh-like pores or dynamic cages at short timescales.[54] In such systems, subdiffusion arises from repeated collisions or entrapment within the surrounding network. At longer timescales, the particles may either escape from the cages if they are smaller than the characteristic pore size, or the cage itself may relax or rearrange, as seen in systems with dynamic microstructures such as colloidal gels or semiflexible polymer networks. This transition marks a change in the dominant transport mechanism—from localized hindered diffusion to long-range Brownian motion—and is reflected in a change in the power-law

Open Access Article. Published on 18 September 2025. Downloaded on 2/18/2026 8:59:30 PM.
This article is licensed under a Creative Commons Attribution-NonCommercial 3.0 Unported Licence.

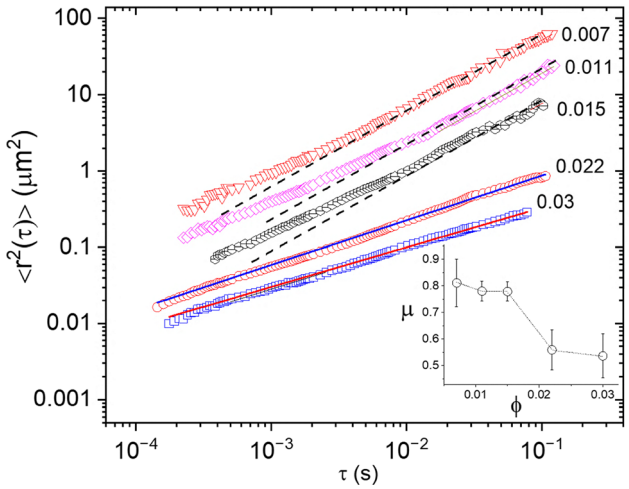

Fig. 3 The log–log plot of mean-square-displacement, $\langle r^2(\tau)\rangle$ *vs.* lag time of nanorods in BSM solutions. The graphs have been shifted vertically for clarity. The different volume fractions were as indicated next to the data. The dashed lines for the three lowest concentrations have a slope of 1 and showed the transition from subdiffusive motion at short time to normal diffusion at long time. There was no subdiffusion observed for the two higher concentration solutions within the experimental time range. (inset) The short-time subdiffusive exponent for different concentrations.

scaling of the MSD from $\langle r^2(\tau)\rangle \sim \tau^{\mu}$ (with $\mu < 1$) at short times to linear scaling ($\mu \approx 1$) at long times. The crossover time τ_x in this scenario corresponds to the timescale at which a particle's displacement exceeds the local confinement scale, and the corresponding crossover length scale is typically on the order of or slightly larger than the mesh size (ξ) of the medium.

Similar behavior has been observed near the sol–gel transition,[55] where increasing cross-linking density leads to a more constrained network. In these systems, nanorods display subdiffusive motion at short lag times due to local confinement by the growing network, followed by a crossover to nearly free diffusion at longer times. However, as cross-linking increases further and the network becomes increasingly rigid, the MSD exhibits persistent subdiffusion across all accessible timescales, indicating that the system has reached the critical gel point. At this point, the network becomes effectively percolated, and the nanorods are permanently restricted by the elastic constraints of the surrounding matrix. This behavior—transitioning from dual-regime diffusion to persistent subdiffusion—is a hallmark of systems approaching gelation or dynamic arrest.

As mentioned previously, although the mucin solutions are in the semidilute regime, they remain unentangled due to the heavy side chains and the absence of long, flexible backbone segments required for topological entanglement. In such systems, there are no well-defined static pores or permanent network structures. Nevertheless, nanoparticles may still experience transient caging or confinement due to local crowding and fluctuating polymer density. These transient cages can momentarily hinder particle motion, leading to subdiffusive dynamics at short timescales. As the polymer configuration fluctuates and relaxes, the particle may escape confinement, giving rise to a crossover to normal diffusion at longer times.

To capture this behavior phenomenologically, we employed a simplified analytical model that assumes confined diffusion at short times and free diffusion at long times, based on particles hopping between semi-permeable cages of uniform size.[56] The model expresses the MSD as: $\langle r^2(\tau)\rangle = L^2(1 - \exp(-\tau/\tau_{eq}))/3 + 4D_M t$ with L representing the effective cage size, τ_{eq} the equilibration time in the domain, and D_M the long-time diffusion coefficient governed by the effective viscosity of the medium. While this model captures the general trend of the crossover in some systems like in agarose gel,[51] in our system the fit deviates significantly at short timescales (Fig. S5). Moreover, the extracted cage size from the fit, $L \approx 0.5\,\mu m$, is unrealistically large relative to the nanorod dimensions. This discrepancy suggests that the assumption of a single dominant structural length scale is not applicable to our system. While transient caging cannot be entirely ruled out as large mucin molecules can wrap around the nanorods,[4] our data indicates that a more appropriate model would involve a broad distribution of local polymer densities, cage lifetimes, and scale dependent confinement as expected in complex systems such as mucin.

Due to PEG-carboxyl functionalization, the zeta potential of the nanorods (NRs) was measured to be ≈–14 mV, indicating a net negative surface charge (Fig. S2). BSM, including its major component MUC5B, is also overall negatively charged, primarily because of its dense array of sugar chains containing carboxyl and sulfate groups. However, despite this net negative charge, MUC5B contains positively charged domains within its protein backbone, which can introduce electrostatic interactions with negatively charged species. In addition, mucins can be regarded as block copolymer – like macromolecules, containing heavily glycosylated, negatively charged regions along with positively charged amino acid domains.[14] Accordingly, the interaction between PEG-coated nanoparticles and mucin is expected to be heterogeneous, involving contributions from electrostatic, hydrophobic, and van der Waals forces. However, our experimental observations provide no evidence of long-lived or stable binding. If such strong or persistent complexes were present, we would expect to see a much substantial decrease in both translational and rotational diffusion coefficients or the appearance of a second, slower diffusing component in the FCS autocorrelation functions—none of which are observed.

Instead, we propose that the observed subdiffusive behavior arises from short-lived, transient interactions, in which nanorods dynamically associate and dissociate with mucin chains as they diffuse through the medium and traverse the FCS detection volume. If the binding/unbinding timescale is on the order of the residence time of the tracer in the focal volume ($\langle\tau_c\rangle \approx$ 10 ms at $\phi = 0.03$), they can introduce an apparent delay that distorts the ACF.[31] In simplified systems, such effects have been modeled using the stick-and-diffuse framework, where tracers undergo rapid binding and unbinding to immobile traps.[50] However, no analytical models currently exist for the case of mobile traps, such as flexible, diffusing polymer chains.

During the transient interactions, the nanorods can temporarily adhere to or be hindered by local polymer segments.

 This journal is © The Royal Society of Chemistry 2025

Open Access Article. Published on 18 September 2025. Downloaded on 2/18/2026 8:59:30 PM. This article is licensed under a Creative Commons Attribution-NonCommercial 3.0 Unported Licence.

These short-lived associations cause the nanorods to intermittently track the local relaxation dynamics of the polymer causing their motion to be coupled with segmental relaxation.[57] In semiflexible polymers such as mucins, local segmental fluctuations are suppressed in amplitude compared to flexible coils, and long-wavelength bending modes relax more slowly. As a result, interactions with embedded particles can persist for longer times than in flexible polymer solutions. In addition, the large persistence length, comparable to rod diameter can promote binding. This coupling of motion results in subdiffusive behavior,[4,58] where the MSD scales as $\langle r^2(t)\rangle \sim t^{\mu}$ with $\mu < 1$. In the Rouse model of polymer dynamics, where the hydrodynamic interactions are neglected, the relaxation times of the chain modes follow a power-law spectrum, with the MSD scaling as $\langle r^2(t)\rangle \sim t^{1/2}$. When hydrodynamic interactions are included, as in the Zimm model,[49] the MSD scales as $\langle r^2(t)\rangle \sim t^{2/3}$. In our experiments, the observed MSD exponent decreases from $\sim$0.8 to $\sim$0.55 as the mucin concentration increases, suggesting a transition from dynamics resembling Zimm behavior toward a more Rouse-like regime as crowding increases and hydrodynamic screening becomes more pronounced.[59] Thus, in the coupled regime, the particle's motion no longer reflects purely Brownian diffusion through a viscous medium but is instead governed by the dynamic properties of the polymer chain itself.

Alternately, the gradual decrease in the exponent with concentration can be explained originating from steric hindrance, which can intermittently constrain the particle's motion. These events can also effectively couple the translational dynamics of the nanorods to the segmental relaxation dynamics of the mucin chains. As the frequency and duration of such constraints increase with polymer concentration, the tracer becomes more sensitive to the internal relaxation spectrum of the network, leading to anomalous diffusion with sublinear scaling. This situation differs from the classical Zimm or Rouse limits, which assume full hydrodynamic coupling or complete screening, respectively. Instead, the system exhibits intermediate scaling, where the MSD exponent reflects a continuum of coupling strengths. Thus, the observed reduction in the MSD exponent with mucin concentration may also reflect a stronger coupling rather than a strict hydrodynamic screening transition.

The transition from subdiffusive motion at short times to normal (Fickian) diffusion at longer times for lower volume fractions is consistent with the scenario well described by the ''vehicle'' model of nanoparticle diffusion.[60] In this framework, at short timescales, the motion of the nanoparticle is coupled to the subdiffusive segmental dynamics of the polymer chains. The nanorod essentially moves along with the polymer, which serves as a temporary ''vehicle.'' After a characteristic desorption time τ_{des}, the nanorod detaches and rebinds to a different polymer segment, initiating a new round of motion. Repetition of these stochastic binding–unbinding events effectively randomizes the trajectory, leading to normal diffusion on longer timescales ($t > \tau_{des}$).[57] In our system, the crossover time is $\approx$ few ms, which is a plausible estimate for τ_{des} given the weak to moderate transient interactions between the nanorods and positively charged domains in the MUC5B backbone. Thus, the experimentally observed crossover can be understood as the transition from locally constrained, interaction-mediated transport to effectively free diffusion governed by multiple desorption and reattachment events.

The translational motion as observed for nanorods in mucin solutions contrasts in important ways with that seen in canonical crowding systems such as concentrated dextran or globular protein solutions.[27,41] In these systems, subdiffusion of spherical tracer particles is typically attributed to excluded volume effects, where increasing macromolecular crowding leads to geometric confinement and restricted access to free volume. Both experiments[41,43,50] and simulations[27] have shown that as the volume fraction of dextran increases, the diffusion coefficient decreases sharply, and the MSD exponent α can drop from $\approx$1 in dilute solution to $\approx$0.5 or below at high volume fractions. In contrast, our mucin system exhibits a similar decrease in α with increasing concentration—does so due to coupling to segmental dynamics. Thus, while the apparent subdiffusion exponent is similar, the physical origin of anomalous transport in mucin is fundamentally distinct from that in crowded systems like dextran. or colloidal gels.

In contrast to translation, the rotation probes very local environments, comparable to the dimensions of the nanorods. For thin rods in polymer solutions, theories predicts that rotational diffusion becomes significantly hindered when the rod length becomes comparable or larger than the entanglement length or tube diameter.[36,61,62] Although our mucin solutions are below full entanglement, the observed sharp, threshold-like decrease of rotational diffusion for $\phi > 0.015$ is consistent with the theory. Also, the stiff mucin chains do not deform easily around the rod and thus act as hard obstacles, which are more persistent in time and space effectively increasing the rotational drag on the rod.

The mean-square angular displacement (MSAD) can be extracted from the short-time decay of the normalized FCS curves, by using the relation. $\langle\theta^2(\tau)\rangle = -\frac{2}{3}\ln G_r(\tau)$. In Fig. 4, we present the MSAD as a function of lag times; the curves have been vertically shifted for clarity. As shown, the MSAD exhibits a clear power-law dependence, $\langle\theta^2(\tau)\rangle \sim \tau$, at short time scales ($\tau < 100$ μs) for all concentrations, indicative of normal diffusive scaling in this regime. This behavior suggests that, on short timescales, the nanorods experience locally homogeneous environments, where rotational dynamics are not significantly hindered by large-scale polymer structure. From this behavior, a short-time rotational correlation time, denoted as τ_r can be estimated using the relation: $\langle\theta^2(\tau)\rangle = \tau/\tau_{r,short}$. The estimated rotational correlation time, τ_r, is approximately 5 μs in buffer, corresponding to the time required for angular displacements on the order of 1 rad^2. At the highest concentration, ϕ = 0.03, $\tau_r \approx$ 17 μs. Therefore, the observation of normal scaling in MSAD up to $\sim$100 μs, which is about 5 times the typical τ_r, the nanorods are only beginning to explore the surrounding microenvironment (less than half a rotation using diffusive scaling).

Open Access Article. Published on 18 September 2025. Downloaded on 2/18/2026 8:59:30 PM.
This article is licensed under a Creative Commons Attribution-NonCommercial 3.0 Unported Licence.

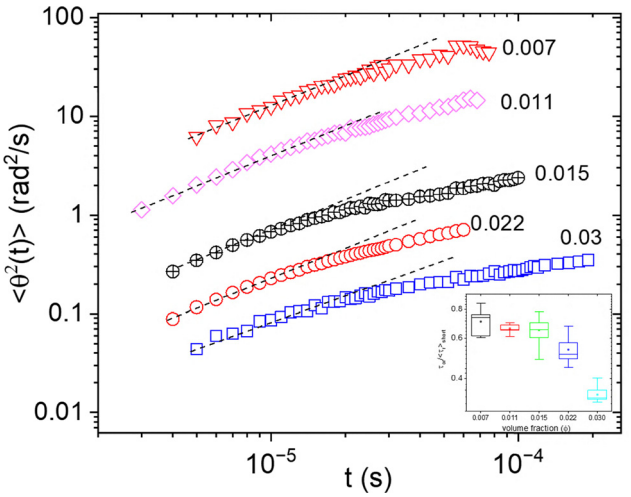

Fig. 4 The mean-square-angular displacement (MSAD) *vs.* lag time extracted from the rotational part of the correlation function. The graphs have been shifted vertically for clarity. The dashed lines have slope of 1. The corresponding volume fractions are indicated. (inset) The relative slow down of short-time rotational diffusion coefficient compared to buffer for different concentration.

In the inset of Fig. 4, we showed the relative slowdown of mean rotational motion—quantified as the ratio of $\tau_{r,short}$ to its value in buffer($\approx$5 μs) as a function of mucin concentration. This analysis allows us to isolate the impact of increasing polymer content on short-time rotational dynamics. Despite this normal diffusive behavior, we observe a slowdown in the overall rotational diffusion coefficient as mucin concentration increases. At higher volume fractions ($\phi \geq 0.021$) the ratio decreases significantly—by several-fold relative to its value in neat buffer. This increase is possible due to combined effects of enhanced hydrodynamic screening, steric hindrance, and frequently more transient interactions with mucin chains. Given the bottlebrush architecture of MUC5B, the rotational motion is more susceptible to obstruction than translation, especially as rod-like tracers reorient over length scales comparable to the local mesh size or persistence length of the mucin filaments. This also explains a decreasing stretched exponential exponent (β) with mucin concentrations (Fig. 2). There is an increase of local heterogeneity, especially at higher concentrations, when mucin forms a denser and more overlapping mesh associated with structural and dynamical heterogeneity. There can be clusters, some areas more gel-like formed by disulfide crosslinking or ionic interaction, others more liquid-like. Thus, rod encounter regions of varying environments resulting in a broad spectrum of relaxation times.

The mesh size ξ of a semiflexible polymer solution can be estimated using a scaling expression[49] that incorporates chain stiffness: $\xi \sim b\phi^{-\frac{3}{4}}\left(\frac{L_p}{b}\right)^{1/4}$, where $b \approx 1$ is the Kuhn segment length and $L_p \approx 15$ nm is the persistence length of the glycosylated regions of mucin. For $\phi = 0.03$ it yields an estimate of mesh size $\xi \approx 27$ nm. According to scaling arguments for rotational diffusion in polymer networks,[36,61] the rotational diffusion coefficient of a nanorod of length L is expected to be suppressed by a factor of $(\xi/L)^3$ compared to its value in dilute buffer. Using the hydrodynamic length of the nanorod obtained from FCS measurements, this predicts a reduction by a factor of approximately 0.25, which is consistent with the experimentally observed trend.

4. Summary and conclusion

In this study, we investigated the rotational and translational dynamics of gold nanorods (AuNRs) in semidilute solutions of bovine submaxillary mucin (BSM), a biologically relevant bottlebrush polymer rich in MUC5B. Using fluctuation correlation spectroscopy (FCS), we measured how mucin concentration modulates nanoparticle motion, revealing complex, concentration-dependent subdiffusive behavior in both translational and rotational motion.

A key finding of our work is the decoupling between translational and rotational dynamics of the nanorods. Here, "decoupling" refers to translational and rotational diffusion exhibiting distinct frictional responses, and should not be confused with the traditional translational–rotational coupling described in scattering studies.[63] While translational motion exhibited only moderate slowing with increasing mucin concentration, rotational diffusion was much more severely hindered especially at higher concentrations. This differential suppression cannot be adequately explained by conventional obstruction or hydrodynamic drag models alone. We attribute the relatively weak impact on translation to transient coupling with segmental dynamics of the semiflexible mucin chains. In this regime, nanorods undergo short-time subdiffusion as they interact with dynamic polymer segments, but at longer timescales, these interactions relax, allowing near-normal translational diffusion. In contrast, rotational motion is more sensitive to local confinement and heterogeneity within the mucin network. As the mucin volume fraction increases, the local environment experienced by a rotating nanorod becomes more restrictive, resulting in a steeper suppression of rotational mobility and a stronger deviation from Brownian behavior.

Our results highlight the distinctive microstructural features of mucin, which differ significantly from conventional crowders such as dextran or globular protein solutions. Unlike these systems, which typically produce isotropic crowding effects dominated by excluded volume interactions, mucin introduces hierarchical constraints and heterogeneous binding domains. This added complexity leads to a richer and more nuanced dynamic landscape, particularly evident when probed with anisotropic tracers such as nanorods. Overall, our findings underscore the importance of probe geometry and polymer architecture in interpreting diffusion measurements in biological and soft matter systems. Anisotropic probes like nanorods are particularly sensitive to multiscale heterogeneities, and their differential responses in translation and rotation offer a powerful window into the structure and dynamics of complex polymer matrices like mucin.

This journal is © The Royal Society of Chemistry 2025

Open Access Article. Published on 18 September 2025. Downloaded on 2/18/2026 8:59:30 PM. This article is licensed under a Creative Commons Attribution-NonCommercial 3.0 Unported Licence.

Conflicts of interest

There are no conflicts to declare.

Data availability

All data supporting the findings of this study are included in the manuscript and the accompanying supplementary information (SI). Supplementary information: TEM image of nanorods, FCS autocorrelation function for nanorods in water with histogram, DLS spectra of mucin in water, MSD as a function of time fitted with a caging model, Zeta potential of nanorods. See DOI: **https://doi.org/10.1039/d5sm00742a**.

Acknowledgements

Acknowledgements are made to the National Science Foundation through Grant CBET-2115827.

References

1 F. Babayekhorasani, D. E. Dunstan, R. Krishnamoorti and J. C. Conrad, *Soft Matter*, 2016, **12**, 8407–8416.
2 R. Chen, R. Poling-Skutvik, M. P. Howard, A. Nikoubashman, S. A. Egorov, J. C. Conrad and J. C. Palmer, *Soft Matter*, 2019, **15**, 1260–1268.
3 J. Hansing and R. R. Netz, *Macromolecules*, 2018, **51**, 7608–7620.
4 F. B. Khorasani, R. Poling-Skutvik, R. Krishnamoorti and J. C. Conrad, *Macromolecules*, 2014, **47**, 5328–5333.
5 C. H. Lee, A. J. Crosby, T. Emrick and R. C. Hayward, *Macromolecules*, 2014, **47**, 741–749.
6 H.-X. Zhou, G. Rivas and A. P. Minton, *Annu. Rev. Biophys.*, 2008, **37**, 375–397.
7 A. G. Cherstvy and R. Metzler, *Soft Matter*, 2019, **15**, 2526–2551.
8 Y. Cu and W. M. Saltzman, *Nat. Mater.*, 2009, **8**, 11–13.
9 K. Khanvilkar, M. Donovan and D. Flanagan, *Adv. Drug Delivery Rev.*, 2001, **48**, 173–193.
10 S. K. Lai, Y. Y. Wang, D. Wirtz and J. Hanes, *Adv. Drug Delivery Rev.*, 2009, **61**, 86–100.
11 O. Lieleg, I. Vladescu and K. Ribbeck, *Biophys. J.*, 2010, **98**, 1782–1789.
12 C. E. Wagner, B. S. Turner, M. Rubinstein, G. H. McKinley and K. Ribbeck, *Biomacromolecules*, 2017, **18**, 3654–3664.
13 B. Button, L.-H. Cai, C. Ehre, M. Kesimer, D. B. Hill, J. K. Sheehan, R. C. Boucher and M. Rubinstein, *Science*, 2012, **337**, 937–941.
14 R. Bansil and B. S. Turner, *Curr. Opin. Colloid Interface Sci.*, 2006, **11**, 164–170.
15 C. R. Gareth, W. Hughes, R. Collins, A. Roseman, R. Ford and D. J. Thornton, *Sci. Rep.*, 2019, **9**, 17350.
16 A. Mukhopadhyay, *Macromolecules*, 2025, **58**, 968–979.
17 T. Odijk, *Macromolecules*, 1983, **16**, 1340–1344.
18 M. D. A. S. F. Edwards, *The Theory of Polymer Dynamics*, Oxford University Press, 1986, Clarendon Press, 1988.
19 P. S. R. Randy Cush, Z. Kucukyavuz, Z. Bu, D. Neau, D. Shih, S. Kucukyavuz and H. Ricks, *Macromolecules*, 1997, **30**, 4920–4926.
20 S. Alam and A. Mukhopadhyay, *Macromolecules*, 2014, **47**, 6919–6924.
21 F. S. Samghabadi, A. H. Slim, M. W. Smith, M. Chabi and J. C. Conrad, *Macromolecules*, 2022, **55**, 10694–10702.
22 M. Smith, R. Poling-Skutvik, A. H. Slim, R. C. Willson and J. C. Conrad, *Macromolecules*, 2021, **54**, 4557–4563.
23 K. A. Rose, N. Gogotsi, J. H. Galarraga, J. A. Burdick, C. B. Murray, D. Lee and R. J. Composto, *Macromolecules*, 2022, **55**, 8514–8523.
24 G. Vicidomini, H. Ta, A. Honigmann, V. Mueller, M. P. Clausen, D. Waithe, S. Galiani, E. Sezgin, A. Diaspro, S. W. Hell and C. Eggeling, *Nano Lett.*, 2015, **15**, 5912–5918.
25 J. W. Miaorong Yu, Y. Yang, C. Zhu, Q. Su, S. Guo, J. Sun, Y. Gan, X. Shi and H. Gao, *Nano Lett.*, 2016, **16**, 7176–7182.
26 Y. L. Binghui Xue, Y. Tian and P. Yin, *Nat. Commun.*, 2024, **15**, 6502.
27 J. Szymanski and M. Weiss, *Phys. Rev. Lett.*, 2009, **103**, 038102.
28 K. Joyner, D. Song, R. F. Hawkins, R. D. Silcotta and G. A. Duncan, *Soft Matter*, 2019, **15**, 9632–9639.
29 R. Omari, A. Aneese, C. Grabowski and A. Mukhopadhyay, *J. Phys. Chem. B*, 2009, **113**, 8449.
30 H. Li, K. Zheng, J. Yang and J. Zhao, *ACS Omega*, 2020, **5**, 11123–11130.
31 R. R. Apostolos Vagias, K. Koynov, U. Jonas, H.-J. Butt, G. Fytas, P. Košovan, O. Lenz and C. Holm, *Phys. Rev. Lett.*, 2013, **111**, 088301.
32 J. M. Tsay, S. Doose and W. Weiss, *J. Am. Chem. Soc.*, 2006, **128**, 1639–1647.
33 S. Rathgeber, H.-J. Beauvisage, H. Chevreau, N. Willenbacher and C. Oelschlaeger, *Langmuir*, 2009, **25**, 6368–6376.
34 M. D. Ediger, *Annu. Rev. Phys. Chem.*, 2000, **51**, 99–128.
35 E. A. Mehdi Molaei and J. C. Crocker, *Phys. Rev. Lett.*, 2018, **120**, 118002.
36 J. Wang, T. C. O'Connor, G. S. Grest, Y. Zheng, M. Rubinstein and T. Ge, *Macromolecules*, 2021, **54**, 7051–7059.
37 C. A. Grabowski and A. Mukhopadhyay, *Macromolecules*, 2014, **47**, 7238–7242.
38 T. G. Mason and D. A. Weitz, *Phys. Rev. Lett.*, 1995, **74**, 1250–1253.
39 U. Yamamoto and K. S. Schweizer, *J. Chem. Phys.*, 2011, **135**, 224902.
40 L. Masaro and X. X. Zhu, *Prog. Polym. Sci.*, 1999, **24**, 731–775.
41 D. S. Banks and C. Fradin, *Biophys. J.*, 2005, **89**, 2960–2971.
42 G. Guigas and M. Weiss, *Biophys. J.*, 2008, **94**, 90–94.
43 M. Weiss, M. Elsner, F. Kartberg and T. Nilsson, *Biophys. J.*, 2004, **87**, 3518–3524.
44 K. K. Senanayake and A. Mukhopadhyay, *Langmuir*, 2019, **35**, 7978–7984.
45 R. I. Cukier, *Macromolecules*, 1984, **17**, 252–255.
46 I. Kohli and A. Mukhopadhyay, *Macromolecules*, 2012, **45**, 6143–6149.

Open Access Article. Published on 18 September 2025. Downloaded on 2/18/2026 8:59:30 PM.
This article is licensed under a Creative Commons Attribution-NonCommercial 3.0 Unported Licence.

47 K. Streletzky and G. D. J. Phillies, *J. Chem. Phys.*, 1988, **108**, 2975–2988.
48 N. J. P. Bruno Zappone, J. B. Madsen, K. I. Pakkanen and S. Lee, *Langmuir*, 2015, **31**, 4524–4533.
49 M. Rubinstein and R. H. Colby, *Polymer physics*, Oxford University Press, New York, 2003.
50 D. S. Banks, C. Tressler, R. D. Peters, F. Höfling and C. C. Fradin, *Soft Matter*, 2016, **12**, 4190–4203.
51 M. D. N. Stolle and C. e Fradin, *Biophys. J.*, 2019, **116**, 791–806.
52 B. B.-C. M. J. Sánchez-Miranda, E. Sarmiento-Gómez, E. Lázaro-Lázaro, A. Ramírez-Saito, M. Medina-Noyola and J. L. Arauz-Lara, *Soft Matter*, 2015, **11**, 655–658.
53 M. L. G. I. Y. Wong, D. R. Reichman, E. R. Weeks, M. T. Valentine, A. R. Bausch and D. A. Weitz, *Phys. Rev. Lett.*, 2004, **92**, 178101.
54 J. Lee, A. Grein-Iankovski, S. Narayanan and R. L. Leheny, *Macromolecules*, 2017, **50**, 406–415.
55 Z. W. Hua Sun and Y. He, *ACS Nano*, 2019, **13**, 11334–11342.
56 M. J. Saxton, *Biophys. J.*, 2008, **95**, 3117–3119.
57 U. Yamamoto, J.-M. Y. Carrillo, V. Bocharova, A. P. Sokolov, B. G. Sumpter and K. S. Schweizer, *Macromolecules*, 2018, **51**, 2258–2267.
58 L.-H. Cai, S. Panyukov and M. Rubinstein, *Macromolecules*, 2011, **44**, 7853–7863.
59 C. K. Gernot Guigas and M. Weiss, *Biophys. J.*, 2007, **93**, 316–323.
60 B. Carroll, V. Bocharova, J.-M. Y. Carrillo, A. Kisliuk, S. Cheng, U. Yamamoto, K. S. Schweizer, B. G. Sumpter and A. P. Sokolov, *Macromolecules*, 2018, **51**, 2268–2275.
61 M. Doi and S. F. Edwards, *J. Chem. Soc., Faraday Trans.*, 1978, **74**, 560–570.
62 K. I. Morozov and A. M. Leshansky, *Macromolecules*, 2022, **55**, 3116–3128.
63 R. P. Sergio and R. Aragón, *J. Chem. Phys.*, 1985, **82**, 5346–5353.

 This journal is © The Royal Society of Chemistry 2025